

## Supporting Information

# Larger-than-Unity External Optical Field Confinement Enabled by Metamaterial-Assisted Comb Waveguide for Ultrasensitive Long-Wave Infrared Gas Spectroscopy

*Weixin Liu,<sup>†,‡,⊥</sup> Yiming Ma,<sup>†,‡,⊥</sup> Xinmiao Liu,<sup>†,‡</sup> Jingkai Zhou,<sup>†,‡</sup> Cheng Xu,<sup>†,‡</sup> Bowei Dong,<sup>†,‡</sup> and  
Chengkuo Lee<sup>\*,†,‡</sup>*

<sup>†</sup>Department of Electrical and Computer Engineering, National University of Singapore,  
Singapore 117583, Singapore

<sup>‡</sup>Center for Intelligent Sensors and MEMS (CISM), National University of Singapore, Singapore  
117608, Singapore

<sup>⊥</sup>W.L. and Y.M. contributed equally.

\*Email: [elelc@nus.edu.sg](mailto:elelc@nus.edu.sg)

## Supplementary note 1: Equivalent RI of SWG metamaterials

Periodic subwavelength grating (SWG) metamaterials provide a flexible approach to engineer the effective index, mode profile, and dispersion of waveguides.<sup>1,2</sup> For SWG metamaterial structure with the periodicity much smaller than the Bragg diffraction regime, equivalent RI is given by:<sup>3</sup>

$$n_{\text{eff}} = \frac{cK}{\omega} \quad (\text{S1})$$

$$\cos(KA) = \cos(k_1 W_s) \cos(k_2 (A - W_s)) - \Delta \sin(k_1 W_s) \sin(k_2 (A - W_s)) \quad (\text{S2})$$

$$\Delta = \frac{1}{2} \left( \frac{k_2}{k_1} + \frac{k_1}{k_2} \right) \quad (\text{S3})$$

$$k_1 = \sqrt{\left( \frac{\omega}{c} n_{\text{Si}} \right)^2 - \beta^2} \quad (\text{S4})$$

$$k_2 = \sqrt{\left( \frac{\omega}{c} n_{\text{air}} \right)^2 - \beta^2} \quad (\text{S5})$$

where  $c$  is the speed of light in vacuum,  $K$  is the Block wave number,  $\omega$  is the angular frequency of the electromagnetic (EM) wave determined by the wavelength,  $W_s$  is the width of Si beam, and  $A$  is the SWG period (At the core region, the period is reduced to  $A/2$ ).  $k_1$  and  $k_2$  are wave vectors of Si slab mode and air along the propagation direction, while  $n_{\text{Si}}$  and  $n_{\text{air}}$  are the corresponding effective index (in our case  $n_{\text{Si}} = 2.9$  and  $n_{\text{air}} = 1$ ), respectively.  $\beta$  represents the projection of the wave vector along the boundary plane, which equals 0 since normal incidence is assumed in our study. Given Eqs. (S1)-(S5), we notice that  $n_{\text{eff}}$  is determined by both period  $A$  and duty cycle ( $W_s/A$  at the cladding and  $2W_s/A$  at the core) of the SWG metamaterial structure. Therefore, the variation of equivalent RI of SWG to its period and duty cycle is calculated, as depicted in Figure S1. In our all-dielectric metamaterial-assisted comb (ADMAL) waveguide, the waveguide and its

surroundings can be divided into three regions. That is, the SWG core, lateral SWG claddings, and top/bottom air claddings, as shown in Figure S1a. The corresponding equivalent RIs at SWG core ( $n_1$ ) and SWG claddings ( $n_2$ ) are given in Figure S1b and S1c, respectively, indicating an always larger equivalent RI at the core region, which is also less susceptible to the period variation as it operates in the deep-subwavelength regime. The RI contrast between the core and lateral claddings ( $n_{\text{cont}} = n_1 - n_2$ ) is further calculated, as depicted in Figure S1d, presenting an obvious parameter dependency to the period and the duty cycle. Moreover, the significantly smaller RI contrast in the lateral direction ( $n_{\text{cont}}$ ) than that in the vertical direction ( $n_1 - n_{\text{air}}$ ) enables the light guiding in our ADMAC waveguide with weaker confinement, but meanwhile, a negligible substrate leakage.

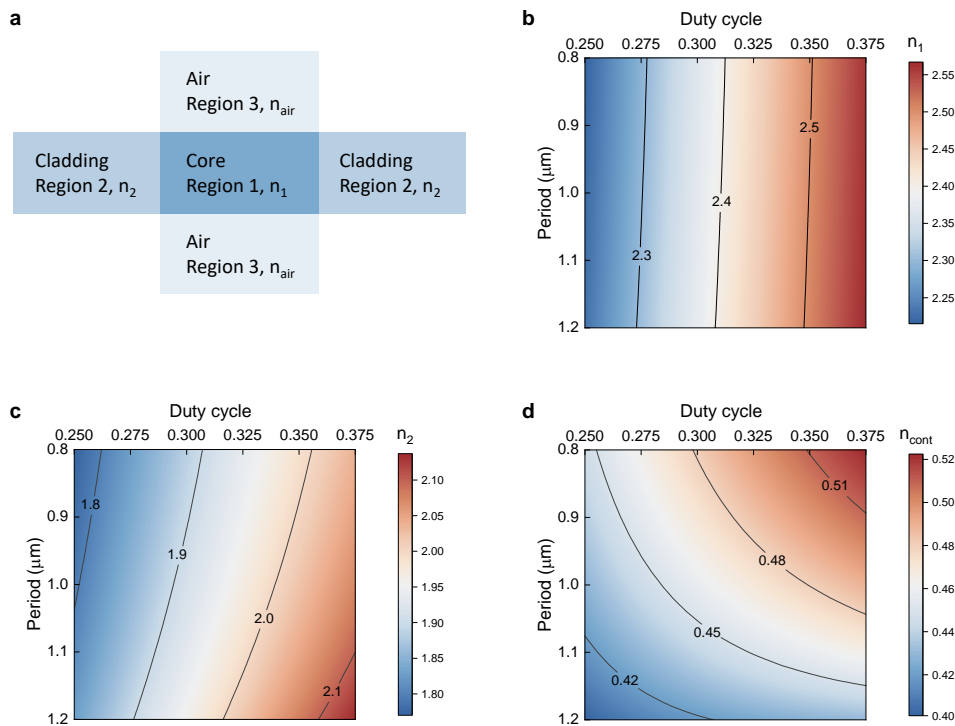


**Figure S1.** Equivalent RIs in ADMAC waveguides. (a) Schematic illustration of the equivalent RIs in comb waveguide configuration. The equivalent RIs in (b) the core region and (c) lateral cladding regions. (d) The RI contrast in the lateral direction.

## Supplementary note 2: Electric field in ADMAC waveguide

As shown in Figure S2, for the light passing through an interface between two lossless dielectric layers (no charge, no current at the interface), Maxwell's equations give relations of electric flux density  $D$  and electric field intensity  $E$  as follows:

$$\hat{n} \cdot (D_1 - D_0) = \rho_s = 0 \quad (\text{S6})$$

$$\hat{n} \times (E_1 - E_0) = 0 \quad (\text{S7})$$

where  $\hat{n}$  is the normal vector of the interface,  $D_1$  and  $D_0$  are the electric flux density in two dielectric layers, respectively.  $\rho_s$  is the surface charge, which equals 0 in our ADMAC waveguide.  $E_1$  and  $E_0$  are the electric field intensity in two layers, respectively. For quasi-TE mode propagation in our ADMAC waveguide, it presents the major E-field components along the x and y directions. Then we can derive the relations of  $E_x$  and  $E_y$  as follows:

$$\hat{n}_x \cdot (\varepsilon_1 E_{x1} - \varepsilon_0 E_{x0}) = 0 \quad (\text{S8})$$

$$\hat{n}_y \cdot (\varepsilon_1 E_{y1} - \varepsilon_0 E_{y0}) = 0 \quad (\text{S9})$$

$$\hat{n}_x \times (E_{x1} - E_{x0}) = 0 \quad (\text{S10})$$

$$\hat{n}_y \times (E_{y1} - E_{y0}) = 0 \quad (\text{S11})$$

where  $\varepsilon_1$  and  $\varepsilon_0$  are the dielectric constants of Si and air, which equals 11.7 and 1, respectively. The continuity of the normal component of  $D$  introduces large discontinuities of  $E_x$  along the x direction and  $E_y$  along the y direction, as evidenced in Figure 1d and 1e in the main text with simulated distributions of  $|E_x|$  and  $|E_y|$  in our ADMAC waveguide. For  $E_x$  ( $E_y$ ) component, the intensities immediately inside the air  $|x|=x_a^+$  ( $|y|=y_b^+$ ) are  $\varepsilon_1/\varepsilon_0$  times higher than that immediately inside the high-index Si beam  $|x|=x_a^-$  ( $|y|=y_b^-$ ). Importantly,  $E_x$  that strongly confined in the air gap is the propagation wave instead of the evanescent wave, resulting in the field remaining high all

across the air gap without exponential decay. This discontinuity is leveraged in our ADMAC waveguide design to strongly enhance and confine light in the air, and thus leads to the extraordinary external confinement factor  $\Gamma$ .

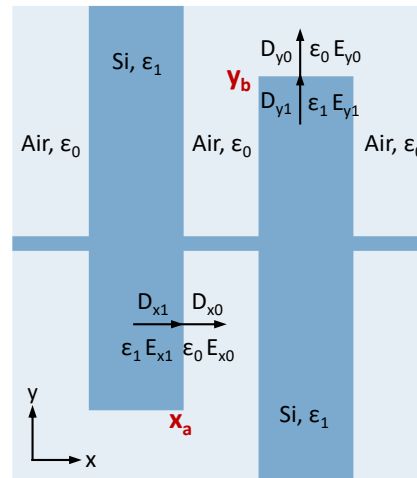


**Figure S2.** Schematic illustration of the ADMAC waveguide structure.

### Supplementary note 3: Simulation of ADMAC waveguide

The group indexes and the spatial electric field distributions of ADMAC waveguides are simulated by the finite difference time domain (FDTD) method in Lumerical. We extracted the corresponding group index ( $n_g = \frac{c}{v_g} = c \frac{\partial k}{\partial \omega}$ , where  $v_g$  is the group velocity) of the guided mode by calculating the inverse gradient  $\frac{\partial k}{\partial \omega}$  in the band diagrams, which give the results presented in Figure 2a in the main text. The 3-dimensional electric field distributions  $E(x, y, z)$  of ADMAC waveguides are extracted with a cubic monitor placed on the propagation path shown in Figure S3. The mesh resolution of this 3-D FDTD simulations is 125 pixels/ $\mu\text{m}$  along the x-direction, 50 pixels/ $\mu\text{m}$  along the y-direction, and 30 pixels/ $\mu\text{m}$  along the z-direction, to ensure the precise extraction of the spatial electrical field distributions  $E(x, y, z)$  of ADMAC waveguides.

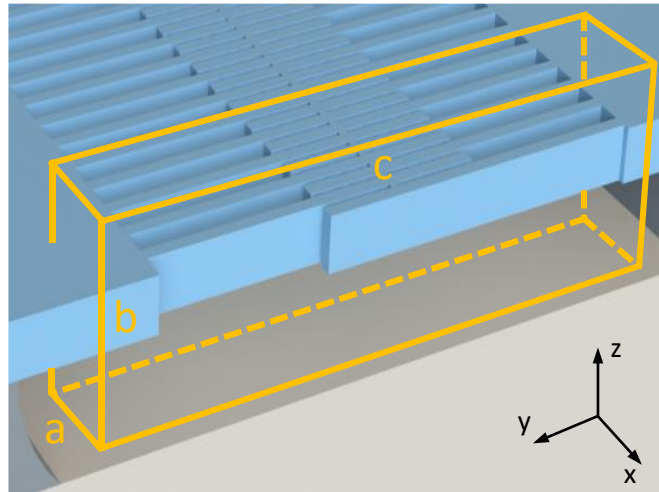


**Figure S3.** Schematic illustration of the simulated box for spatial electrical field distribution, where  $a$  is selected as six comb periods,  $b = 7.5 \mu\text{m}$ ,  $c = 15.5 \mu\text{m}$ .

#### Supplementary note 4: Figure of merit for on-chip IR-TDLAS sensors

For absorption-based waveguide sensors, light is attenuated due to the molecular absorption in the cladding region and the waveguide propagation losses, which can be expressed by the Beer-Lambert law

$$T = \frac{I}{I_0} = e^{-\varepsilon c \Gamma l - \alpha l} \quad (\text{S12})$$

where  $T$  is the transmittance,  $\varepsilon$  is the molar absorption coefficient,  $c$  is the analyte concentration, and  $l$  is the physical waveguide length. Here, the waveguide attenuation coefficient  $\alpha$  accounts for all losses not due to molecular absorption, including material, scattering, and substrate losses, that is, the overall propagation losses as presented in Figure 3b in the main text.

The general goal of waveguide sensors is to maximize the change in fractional optical power, that is,  $1-T$ , induced by the molecular absorption of analytes in the cladding region. Therefore, the waveguide sensitivity is given by:<sup>4</sup>

$$S = \frac{d(1-T)}{dc} = \frac{d}{dc} (1 - e^{-\varepsilon c \Gamma l - \alpha l}) = \varepsilon \Gamma l e^{-\varepsilon c \Gamma l - \alpha l} \quad (\text{S13})$$

In most of the theoretical analyses of waveguide sensors, the noise level is assumed to be a constant value (typically only take account of photodetector noise).<sup>4-9</sup> Consequently, their general goal is to maximize the device sensitivity and from which the optimized waveguide length can be calculated. Nevertheless, the assumption of a constant noise level is not always true, which is likely only valid with an ultralow-noise light source or with an ultralow signal intensity where the photodetector noise dwarfs the contribution of laser power fluctuation. In most cases, laser power fluctuation that is proportional to the light intensity dominates the overall noise. Following we will show that two cases (i)  $I_{\text{noise}} = \text{constant}$ ; (ii)  $I_{\text{noise}} = kI$  (the noise floor is proportional to the signal

intensity received by the photodetector) give different optimized waveguide lengths, while the FOM used in our work gives a good measure of the waveguide sensing performance with regard to the achievable LoD in both two cases.

(i)  $I_{\text{noise}} = \text{constant}$ ;

The sensitivity can be maximized with respect to the waveguide length  $l$ :

$$\frac{dS}{dl} = [1 - l(\varepsilon c \Gamma + \alpha)] \varepsilon \Gamma e^{-\varepsilon c \Gamma l - \alpha l} = 0 \quad (\text{S14})$$

$$l_{\text{opt}} = \frac{1}{\varepsilon c \Gamma + \alpha} \quad (\text{S15})$$

The optimized sensitivity is then given by:

$$S_{\text{opt}} = \frac{\varepsilon \Gamma}{\varepsilon c \Gamma + \alpha} e^{-1} \quad (\text{S16})$$

As the waveguide propagation loss generally is greatly larger than the loss induced by the molecular absorption, the sensitivity can be closely approximated as:

$$S_{\text{opt}} = \frac{\varepsilon \Gamma}{\alpha} e^{-1} \quad (\text{S17})$$

Due to the constant noise floor, the LoD is simply inversely proportional to the sensitivity:

$$\text{LoD} \approx \frac{\text{SNR} \cdot I_{\text{noise}}}{S \cdot I_0} \propto \frac{\alpha}{\varepsilon \Gamma} \quad (\text{S18})$$

(ii)  $I_{\text{noise}} = kI$ ;

In this case, the achievable LoD of waveguide sensors is not necessarily occurred at the maximum sensitivity, which can be rather expressed as:

$$\text{LoD} \approx \frac{\text{SNR} \cdot I_{\text{noise}}}{S \cdot I_0} = \frac{\text{SNR} \cdot kI_0 \cdot e^{-\varepsilon c \Gamma l - \alpha l}}{I_0 \cdot \varepsilon \Gamma l e^{-\varepsilon c \Gamma l - \alpha l}} = \frac{\text{SNR} \cdot k}{\varepsilon \Gamma l_{\text{opt}}} \propto \frac{\alpha}{\varepsilon \Gamma} \quad (\text{S19})$$

where SNR is the signal-to-noise ratio, which is 1 in our work given 1- $\sigma$  criterion. Therefore, a waveguide as long as possible is desired in this case (whenever the assumption  $I_{\text{noise}} = kI$  is still valid).

Importantly, in both two cases, the LoD of waveguide sensors is inversely proportional to the molar absorption coefficient  $\varepsilon$  and  $\Gamma/\alpha$ , while the latter is the FOM used in our work for waveguide sensors that take account of both the per-length light-matter interaction and the waveguide propagation loss. Therefore, this FOM provides a good measure of the achievable LoD of waveguides with different configurations and in different testing conditions.

## Supplementary note 5: Waveguide characterizations and spectroscopic measurements

The waveguide characterization was performed in the spectroscopy setup with the fiber-coupled configuration shown in Figure S4. A continuous-wave quantum cascade laser was employed for the light-emitting and modulated by a chopper. The modulated light was then focused by a ZnSe lens into a hollow fiber, with its polarization controlled by a half-wave plate. The alignment between the fiber and the devices was performed with a six-axis alignment stage. The post-chip light was coupled to another hollow fiber and converted to the electrical signal by a liquid nitrogen-cooled MCT detector. Both the chopper and the detector were connected to a lock-in amplifier to enhance the signal-to-noise ratio. Importantly, to minimize the optical absorption from the ambient environment, the free space optical path was sealed and purged with clean dry air during the whole test.

For the spectroscopic measurements of acetone vapor, nitrogen was selected as the diluting gas, with its overall flow rate controlled by a mass flow controller at 800 mL/min. Then nitrogen was divided into two flows. One was pumped into 99.5% acetone solution to generate an acetone-nitrogen mixture, and the other remained as pure nitrogen. After that, two flows re-mix, and the acetone concentration in the dilution was calibrated by a commercial sensor before being pumped into the gas feeding chamber. The concentration of acetone in the sensing region was precisely and dynamically controlled by regulating the valves in two flows, giving a wide concentration range from several ppm to several thousand ppm.

The free-space reference was measured from Fourier-transform infrared (FTIR) spectrometer with the same gas generation setup and flow rate in waveguide spectroscopic measurements, as shown in Figure S5. Infrared light from FTIR light source was detected by the MCT detector after passing a gas cell with a free space pathlength of 10 mm. On the top and bottom sides of the cell,

there are two  $\text{CaF}_2$  windows for the light passing. The gas cell was first filled with pure nitrogen and the transmission spectrum was measured as the background. Afterward, acetone-nitrogen mixtures with different pre-calibrated acetone concentrations were sent into the gas cell. The transmission spectra with different acetone concentrations were then normalized to the background to extract absorption spectra and give the free-space references presented in Figure 4.

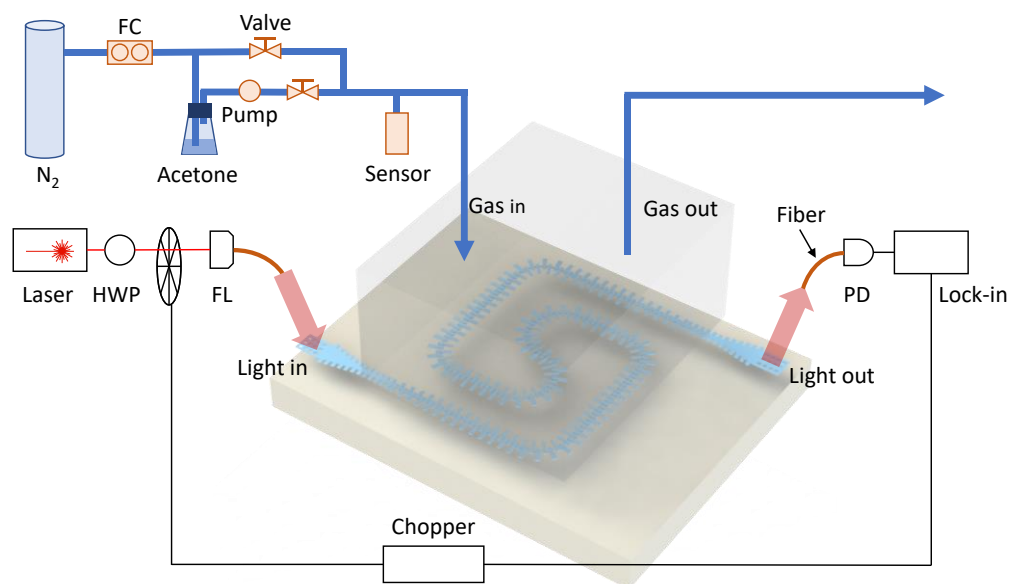


**Figure S4.** Experimental setup for waveguide absorption spectroscopy. FC: flow controller. HWP: half-wave plate. FL: focusing lens. PD: photodetector. The optical path was sealed and purged with clean dry air (not shown).

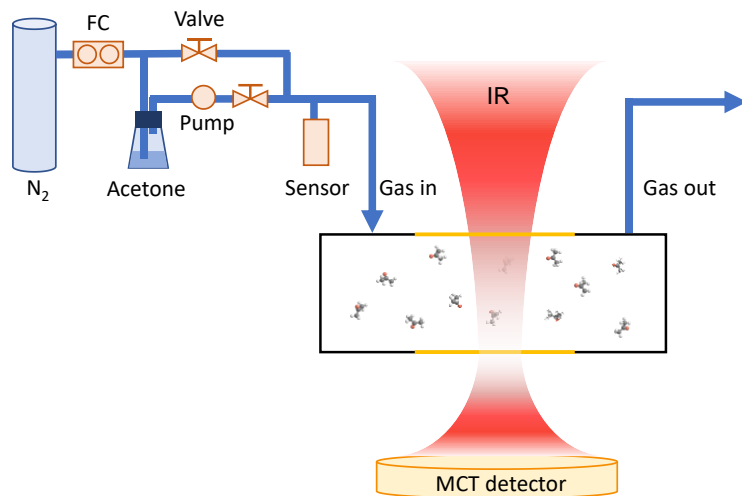


**Figure S5.** Experimental setup for the measurement of free-space references.

## **Supplementary note 6: Waveguide fabrication**

The ADMAC waveguide sensors were built on a commercial SOI wafer with a 1.5- $\mu\text{m}$ -thick device layer and a 3- $\mu\text{m}$ -thick BOX layer. Single-step electronic beam lithography was used to define the waveguide layout in high contrast resist of ZEP-520A, followed by inductively coupled plasma reactive ion etching (ICP-RIE, with  $\text{SF}_6/\text{C}_4\text{F}_8/\text{Ar}$  chemistry) to transfer the pattern onto the device layer. BOX beneath the waveguide was then locally wet etched by hydrofluoric acid (1:5 HF) for 3.5 h to ensure its complete removal under the widest structure. Due to the strong mechanical strength of the comb structure, the critical point drying is not necessary after HF wet etching. During the waveguide fabrication, a 60 nm enlargement of air gaps was observed in the Si dry etching. Therefore, we applied an equal but negative offset in the designed layout for compensation.

## Supplementary note 7: Summary of MWIR/LWIR waveguide platforms

Table S1. Summary of MWIR/LWIR waveguide platforms

Platform	Waveguide configuration	Wavelength ( $\mu\text{m}$ )	Propagation loss (dB/cm)	Bending loss (dB/bend)	Ref
SOI <sup>a</sup>	SWG metamaterial	7.0-7.5	4.7	0.12	This work
SOI <sup>a</sup>	Strip	7.67	3.1	0.08	10
SOI <sup>a</sup>	Strip	6.4 – 6.8	4.3	0.06	11
SOI <sup>a</sup>	Strip	5.3 – 5.7	<2	N/A	12
GOS	Rib	6.7 – 7.45	< 5	N/A	13
GOS	Rib	6.85 – 11.25	< 10	N/A	14
Graded SiGe	Rib	8.5	< 3	N/A	15
GOI <sup>a</sup>	Rib	7.67	2.65	N/A	16
Ge-Sb-Ge	Strip	7.7	2.5	N/A	17
SOCF	Strip	6.3-7.1	4.64	0.05	18
SOCF	Rib	5.1 – 5.3	3.8	< 0.1	19
SOS	Strip	5.4 – 5.6	4.0	N/A	20
Diamond	Strip	5 – 7	~ 5.5	N/A	21
SOI <sup>a</sup>	Strip	4.24	3	N/A	22
SON	Rib	3.39	5.1	N/A	23
GON	Strip	3.73	7.86	N/A	24
SOPS	Strip	3.39	3.9	0.006	25
AlNOI	Strip	3.65 – 3.9	8.2	0.2	26

<sup>a</sup>With a free-standing configuration by undercutting the BOX layer.

<sup>b</sup>GOS: germanium-on-silicon; SOCF: silicon-on-calcium fluoride; SOS: silicon-on-sapphire; SON: silicon-on-nitride; GON: germanium-on-nitride; SOPS: silicon-on-porous-silicon; AlNOI: aluminum nitride-on-insulator.

### Supplementary note 8: Waveguide cutback measurements

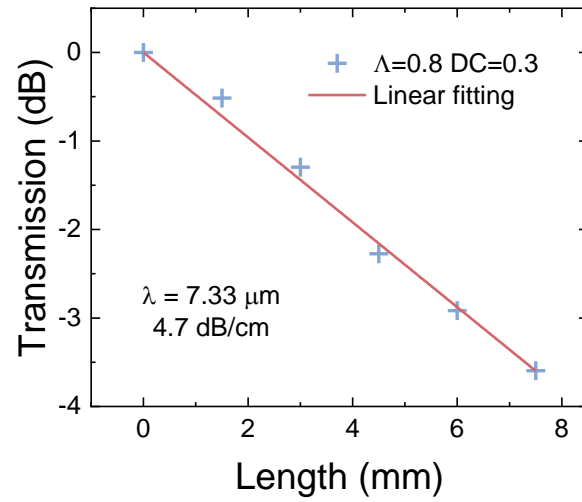


**Figure S6.** Cutback measurements of ADMAC waveguide with a period of 0.8  $\mu\text{m}$  and a duty cycle of 0.3 at 7.33  $\mu\text{m}$ .

## Supplementary note 9: Functional blocks of ADMAC waveguide

In our optical characterization, waveguides were probed in a fiber-coupled configuration with light collected and emitted through on-chip grating couplers (Figure S4). To enable broadband spectroscopic sensing, the grating coupler was designed to provide sufficient coupling efficiency for TE polarized light over our interested wavelength range (7.05-7.5  $\mu\text{m}$ ), as shown in Figure S7a. Figure S7d presents the spectrum of the grating coupler with a measured maximum coupling efficiency of -9 dB. The measured 3-dB bandwidth of 700 nm is well-matched with the simulated results and outperforms those of reported mid-infrared grating couplers (Table S2). The ADMAC waveguide was accessed via 2.5- $\mu\text{m}$ -wide strip waveguides at both ends. Therefore, a mode converter was designed to smoothly convert light from symmetric mode in strip waveguide ( $n_{\text{eff}} = 2.9$ ) to asymmetric and oscillating mode in ADMAC waveguide (Figure S7b). Figure S7e presents the transition losses of the 15- $\mu\text{m}$ -long converter, which are flat over the measured wavelength range and have an average of only 0.11 dB. For longer tapering lengths, the converters present even lower losses due to the smoother mode transitions, as evidenced by the length-dependent loss measurement in the inset of Figure S7e. Our sensing chip also involves 90° bends with a radius of 150  $\mu\text{m}$  to curl the ADMAC waveguide into a spiral for a compact footprint (Figure S7c). The cutback measurements of waveguides with different bend numbers and radii give data presented in Figure S7f and its inset, indicating that a 90° bend possesses only ~0.12 dB loss with a 150  $\mu\text{m}$  radius and maintain this low bending loss with the radius down to 50  $\mu\text{m}$ .

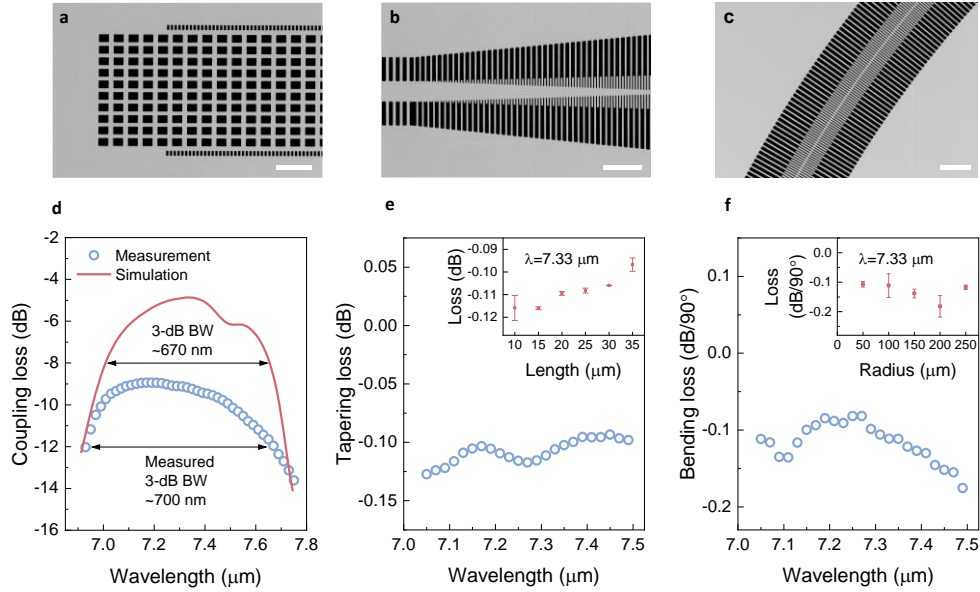


**Figure S7.** Functional blocks of ADMAC waveguide sensor. SEM images of (a) grating coupler, (b) mode converter, and (c) 90° bend. The scale bars are 10  $\mu\text{m}$ , 5  $\mu\text{m}$ , 5  $\mu\text{m}$ , respectively. (d) The simulated and measured spectrum of the grating coupler. BW: bandwidth. (e) Wavelength-dependent loss of mode converter with a length of 15  $\mu\text{m}$ . Inset shows its loss performance with different tapering lengths. (f) Wavelength-dependent bending loss of 90° bend with a radius of 150  $\mu\text{m}$ . Inset shows its loss performance with different bending radii. All these functional blocks have a period of 0.8  $\mu\text{m}$  and a duty cycle of 0.3.

**Supplementary note 10: Summary of MWIR/LWIR grating couplers**

Table S2. Summary of MWIR/LWIR grating couplers

<b>Platform</b>	<b>Central wavelength (<math>\mu\text{m}</math>)</b>	<b>Maximum coupling efficiency (dB)</b>	<b>1-dB bandwidth (nm)</b>	<b>3-dB bandwidth (nm)</b>	<b>Ref</b>
<b>SOI<sup>a</sup></b>	<b>7.3</b>	<b>-9</b>	<b>500</b>	<b>700</b>	<b>This work</b>
GOS	6.95	N/A	N/A	500	13
GOS	5.2	-5	N/A	100	27
GOS	5.2	-4	N/A	180	27
SOI <sup>a</sup>	6.63	-7	170	304	11
SOCF	6.51	-12	N/A	200	18
SOCF	6.61	-9.77	N/A	200	18
SOI	3.75	-7.37	152	263.5	28
SOI	3.68	-6.48	N/A	199	28
SOS	3.43	-5.38	N/A	N/A	29
SOS	2.75	-4.87	N/A	N/A	30
GOI <sup>a</sup>	2.37	-11	58	N/A	31
GOS	3.8	-11	70	N/A	32
GOS	3.8	-16.5	70	N/A	33

<sup>a</sup>With a free-standing configuration by undercutting the BOX layer.

## Supplementary note 11: Noise analysis

In our sensor system, the white noise mainly consists of laser power fluctuation and MCT photodetector noise. This is evidenced by the comparison between system Allan deviation and laser-detector Allan deviation, as presented in Figure S8a (Inset shows the setup for laser-detector Allan deviation measurement). With short averaging times, system Allan deviation is close to laser-detector Allan deviation, indicating that the dominant noise components come from the laser and the photodetector instead of alignment stages. As the averaging time increases, system Allan deviation gradually deviates from laser-detector Allan deviation due to more significant influences of low-frequency drift of alignment stages.

Particularly, the laser power fluctuation is proportional to the laser intensity, while the photodetector noise almost keeps constant regardless of the signal power. To further identify and quantify these two noise components, we characterized the relationship between noise level and signal intensity without time averaging, as plotted in Figure S8b. The slope of the linear fitting suggests that laser power fluctuation occupies  $\sim 0.04\%$  of the signal, while the intercept mainly represents the constant photodetector noise of  $\sim 8 \mu\text{V}$ . Therefore, for our typical measurement with the signal intensity ranging from  $1 \times 10^5 \mu\text{V}$  to  $1 \times 10^6 \mu\text{V}$ , the noise attributed to the laser power fluctuation is around  $40 \mu\text{V} - 400 \mu\text{V}$ . This means most of the measured noises come from the laser power fluctuation, which is the case of measurements in Figure 5b. Consequently, we can expect a sub-ppm LoD for acetone by employing a low-noise laser source and/or adopting fiber-chip packaging without alignment stages in the current experimental setup.<sup>13,34,35</sup>

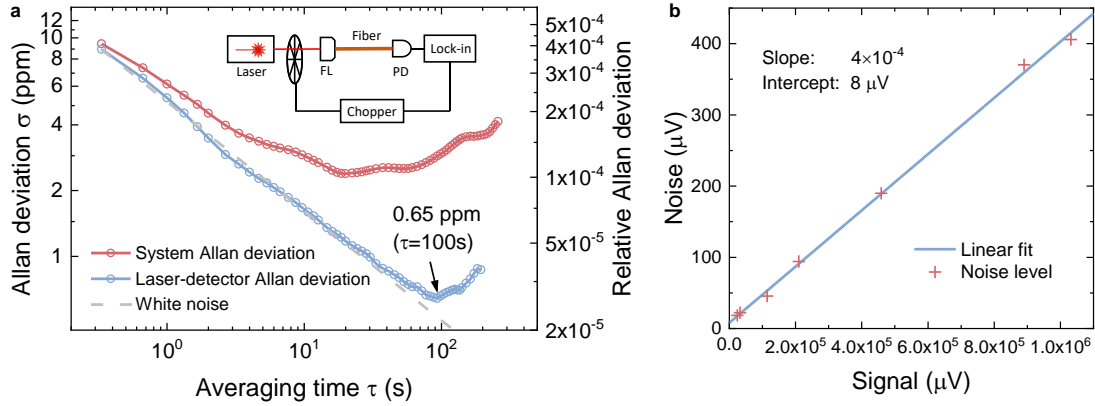


**Figure S8.** Noise analysis of the sensor system. (a) Laser-detector Allan deviation and system Allan deviation as a function of the averaging time  $\tau$ . White noise with a slope of  $\tau^{-1/2}$  is indicated with the dashed line. Inset: the setup for laser-detector Allan deviation measurement. (b) The noise floor as a function of the signal measured in our sensor system without a time-averaging process. The slope of the linear fitting suggests a laser power fluctuation of 0.04% of the signal, and the intercept suggests a constant detector noise of  $\sim 8 \mu\text{V}$ .

## REFERENCES

- (1) Bock, P. J.; Cheben, P.; Schmid, J. H.; Lapointe, J.; Del age, A.; Janz, S.; Aers, G. C.; Xu, D.-X.; Densmore, A.; Hall, T. J. Subwavelength Grating Periodic Structures in Silicon-on-Insulator: A New Type of Microphotonic Waveguide. *Opt. Express* **2010**, *18* (19), 20251–20262.
- (2) Cheben, P.; Halir, R.; Schmid, J. H.; Atwater, H. A.; Smith, D. R. Subwavelength Integrated Photonics. *Nature* **2018**, *560* (7720), 565–572.
- (3) Yariv, A.; Yeh, P. Electromagnetic Propagation in Periodic Stratified Media II Birefringence, Phase Matching, and x-Ray Lasers. *J. Opt. Soc. Am.* **1977**, *67* (4), 438–448.

- (4) Kita, D. M.; Michon, J. J. J. J. J.; Johnson, S. G.; Hu, J.; Johnson, S. G.; Hu, J.; Johnson, S. G.; Hu, J. Are Slot and Sub-Wavelength Grating Waveguides Better than Strip Waveguides for Sensing? *Optica* **2018**, *5* (9), 1046–1054.
- (5) Gutierrez-Arroyo, A.; Baudet, E.; Bodiou, L.; Nazabal, V.; Rinnert, E.; Michel, K.; Bureau, B.; Colas, F.; Charrier, J. Theoretical Study of an Evanescent Optical Integrated Sensor for Multipurpose Detection of Gases and Liquids in the Mid-Infrared. *Sensors Actuators, B Chem.* **2017**, *242*, 842–848.
- (6) Pi, M.; Zheng, C.; Bi, R.; Zhao, H.; Liang, L.; Zhang, Y.; Wang, Y.; Tittel, F. K. Design of a Mid-Infrared Suspended Chalcogenide/Silica-on-Silicon Slot-Waveguide Spectroscopic Gas Sensor with Enhanced Light-Gas Interaction Effect. *Sensors Actuators, B Chem.* **2019**, *297* (June), 126732.
- (7) Yazici, M. S.; Dong, B.; Hasan, D.; Sun, F.; Lee, C. Integration of MEMS IR Detectors with MIR Waveguides for Sensing Applications. *Opt. Express* **2020**, *28* (8), 11524–11537.
- (8) Wang, Y.; Chen, W.; Wang, P.; Dai, S.; Li, J.; Li, Y.; Fu, Q.; Dai, T.; Yu, H.; Yang, J. Ultra-High-Power-Confinement-Factor Integrated Mid-Infrared Gas Sensor Based on the Suspended Slot Chalcogenide Glass Waveguide. *Sensors Actuators B Chem.* **2021**, *347* (August), 130466.
- (9) Kumari, B.; Varshney, R. K.; Pal, B. P. Design of Chip Scale Silicon Rib Slot Waveguide for Sub-ppm Detection of N<sub>2</sub>O Gas at Mid-IR Band. *Sensors Actuators, B Chem.* **2018**, *255* (2), 3409–3416.
- (10) Penadés, J. S.; Sánchez-Postigo, A.; Nedeljkovic, M.; Ortega-Moñux, A.; Wangüemert-

- Pérez, J. G.; Xu, Y.; Halir, R.; Qu, Z.; Khokhar, A. Z.; Osman, A.; Cao, W.; Littlejohns, C. G.; Cheben, P.; Molina-Fernández, I.; Mashanovich, G. Z. Suspended Silicon Waveguides for Long-Wave Infrared Wavelengths. *Opt. Lett.* **2018**, *43* (4), 795–798.
- (11) Liu, W.; Ma, Y.; Chang, Y.; Dong, B.; Wei, J.; Ren, Z.; Lee, C. Suspended Silicon Waveguide Platform with Subwavelength Grating Metamaterial Cladding for Long-Wave Infrared Sensing Applications. *Nanophotonics* **2021**, *10* (7), 1861–1870.
- (12) Duong Dinh, T. T.; Le Roux, X.; Koopai, N.; Melati, D.; Montesinos-Ballester, M.; González-Andrade, D.; Cheben, P.; Velasco, A. V.; Cassan, E.; Marris-Morini, D.; Vivien, L.; Alonso-Ramos, C. Mid-Infrared Fourier-Transform Spectrometer Based on Metamaterial Lateral Cladding Suspended Silicon Waveguides. *Opt. Lett.* **2022**, *47* (4), 810–813.
- (13) Benéitez, N. T.; Baumgartner, B.; Missinne, J.; Radosavljevic, S.; Wacht, D.; Hugger, S.; Leszcz, P.; Lendl, B.; Roelkens, G. Mid-IR Sensing Platform for Trace Analysis in Aqueous Solutions Based on a Germanium-on-Silicon Waveguide Chip with a Mesoporous Silica Coating for Analyte Enrichment. *Opt. Express* **2020**, *28* (18), 27013–27027.
- (14) Kozak, D. A.; Stievater, T. H.; Mahon, R.; Rabinovich, W. S. Germanium-on-Silicon Waveguides at Wavelengths from 6.85 to 11.25 Microns. *IEEE J. Sel. Top. Quantum Electron.* **2018**, *24* (6), 6–9.
- (15) J.M.Ramirez; Q, L.; V.Vakarín; J.Friggerio; A.Ballabio; Roux, X. L.; D.Bouville; L.Vivien; G.Isella; D.Marris-Morini. Graded SiGe Waveguides with Broadband Low-Loss Propagation in the Mid Infrared. *Opt. Express* **2018**, *26* (2), 870–877.

- (16) Osman, A.; Nedeljkovic, M.; Soler Penades, J.; Wu, Y.; Qu, Z.; Khokhar, A. Z.; Debnath, K.; Mashanovich, G. Z. Suspended Low-Loss Germanium Waveguides for the Longwave Infrared. *Opt. Lett.* **2018**, *43* (24), 5997–6000.
- (17) Gutierrez-Arroyo, A.; Baudet, E.; Bodiou, L.; Lemaitre, J.; Hardy, I.; Fajjan, F.; Bureau, B.; Nazabal, V.; Charrier, J. Optical Characterization at 7.7  $\mu\text{m}$  of an Integrated Platform Based on Chalcogenide Waveguides for Sensing Applications in the Mid-Infrared. *Opt. Express* **2016**, *24* (20), 23109–23117.
- (18) Ma, Y.; Chang, Y.; Dong, B.; Wei, J.; Liu, W.; Lee, C. Heterogeneously Integrated Graphene/Silicon/Halide Waveguide Photodetectors toward Chip-Scale Zero-Bias Long-Wave Infrared Spectroscopic Sensing. *ACS Nano* **2021**, *15* (6), 10084–10094.
- (19) Chen, Y.; Lin, H.; Hu, J.; Li, M. Heterogeneously Integrated Silicon Photonics for the Mid-Infrared and Spectroscopic Sensing. *ACS Nano* **2014**, *8* (7), 6955–6961.
- (20) Spott, A.; Liu, Y.; Baehr-Jones, T.; Ilic, R.; Hochberg, M. Silicon Waveguides and Ring Resonators at 5.5  $\mu\text{m}$ . *Appl. Phys. Lett.* **2010**, *97* (21), 213501.
- (21) Haas, J.; Catalán, E. V.; Piron, P.; Nikolajeff, F.; Österlund, L.; Karlsson, M.; Mizaikoff, B. Polycrystalline Diamond Thin-Film Waveguides for Mid-Infrared Evanescent Field Sensors. *ACS Omega* **2018**, *3* (6), 6190–6198.
- (22) Ottonello-Briano, F.; Errando-Herranz, C.; Rödjegård, H.; Martin, H.; Sohlström, H.; Gylfason, K. B. Carbon Dioxide Absorption Spectroscopy with a Mid-Infrared Silicon Photonic Waveguide. *Opt. Lett.* **2020**, *45* (1), 109–112.

- (23) Khan, S.; Chiles, J.; Ma, J.; Fathpour, S. Silicon-on-Nitride Waveguides for Mid- and near-Infrared Integrated Photonics. *Appl. Phys. Lett.* **2013**, *102* (12), 121104.
- (24) Li, W.; Tan, C. S.; Anantha, P.; Lee, K. H.; Qiu, H. D.; Guo, X.; Goh, S. C. K.; Zhang, L.; Wang, H.; Soref, R. A. Spiral Waveguides on Germanium-on-Silicon Nitride Platform for Mid-IR Sensing Applications. *IEEE Photonics J.* **2018**, *10* (3), 2201107.
- (25) Mashanovich, G. Z.; Milošević, M. M.; Nedeljkovic, M.; Owens, N.; Xiong, B.; Teo, E. J.; Hu, Y. Low Loss Silicon Waveguides for the Mid-Infrared. *Opt. Express* **2011**, *19* (8), 7112–7119.
- (26) Dong, B.; Luo, X.; Zhu, S.; Li, M.; Hasan, D.; Zhang, L.; Chua, S. J.; Wei, J.; Chang, Y.; Lo, G.-Q.; Ang, K. W.; Kwong, D.-L.; Lee, C. Thermal Annealing Study of the Mid-Infrared Aluminum Nitride on Insulator (AlNOI) Photonics Platform. *Opt. Express* **2019**, *22* (14), 19815–19826.
- (27) Radosavljevic, S.; Kuyken, B.; Roelkens, G. Efficient 5.2  $\mu\text{m}$  Wavelength Fiber-to-Chip Grating Couplers for the Ge-on-Si and Ge-on-SOI Mid-Infrared Waveguide Platform. *Opt. Express* **2017**, *25* (16), 19034–19042.
- (28) Chen, N.; Dong, B.; Luo, X.; Wang, H.; Singh, N.; Lo, G.; Lee, C. Efficient and Broadband Subwavelength Grating Coupler for 3.7  $\mu\text{m}$  Mid-Infrared Silicon Photonics Integration. *Opt. Express* **2018**, *26* (20), 26242–26256.
- (29) Zou, Y.; Subbaraman, H.; Chakravarty, S.; Xu, X.; Hosseini, A. Grating-Coupled Silicon-on-Sapphire Integrated Slot Waveguides Operating at Mid-Infrared Wavelengths. *Opt. Lett.* **2014**, *39* (10), 3070–3073.

- (30) Cheng, Z.; Chen, X.; Wong, C. Y.; Xu, K.; Fung, C. K. Y.; Chen, Y. M.; Tsang, H. K. Mid-Infrared Grating Couplers for Silicon-on-Sapphire Waveguides. *IEEE Photonics J.* **2012**, *4* (1), 104–113.
- (31) Kang, J.; Cheng, Z.; Zhou, W.; Xiao, T.-H.; Gopalakrisna, K.-L.; Takenaka, M.; Tsang, H. K.; Goda, K. Focusing Subwavelength Grating Coupler for Mid-Infrared Suspended Membrane Germanium Waveguides. *Opt. Lett.* **2017**, *42* (11), 2094–2097.
- (32) Alonso-Ramos, C.; Nedeljkovic, M.; Benedikovic, D.; Penadés, J. S.; Littlejohns, C. G.; Khokhar, A. Z.; Pérez-Galacho, D.; Vivien, L.; Cheben, P.; Mashanovich, G. Z. Germanium-on-Silicon Mid-Infrared Grating Couplers with Low-Reflectivity Inverse Taper Excitation. *Opt. Lett.* **2016**, *41* (18), 4324–4327.
- (33) Nedeljkovic, M.; Soler Penadés, J.; Mitchell, C. J.; Khokhar, A. Z.; Stanković, S.; Dominguez Bucio, T.; Littlejohns, C. G.; Gardes, F. Y.; Mashanovich, G. Z. Surface Grating Coupled Low Loss Ge-on-Si Rib Waveguides and Multimode Interferometers. *Photonics Technol. Lett. IEEE* **2015**, *27* (10), 1040–1043.
- (34) Schwaighofer, A.; Montemurro, M.; Freitag, S.; Kristament, C.; Culzoni, M. J.; Lendl, B. Beyond Fourier Transform Infrared Spectroscopy: External Cavity Quantum Cascade Laser-Based Mid-Infrared Transmission Spectroscopy of Proteins in the Amide I and Amide II Region. *Anal. Chem.* **2018**, *90* (11), 7072–7079.
- (35) Nambiar, S.; Sethi, P.; Selvaraja, S. Grating-Assisted Fiber to Chip Coupling for SOI Photonic Circuits. *Appl. Sci.* **2018**, *8* (7), 1142.